Generation of isolated attosecond soft x-ray pulses using a nondispersive inverse Cherenkov dielectric laser modulator

Liwen Zhang[*]

College of Materials Science and Technology, Nanjing University of Aeronautics and Astronautics, Nanjing 211106, China

Xujun Xu and Weihao Liu[†]

College of Electronic and Information Engineering, Nanjing University of Aeronautics and Astronautics, Nanjing 211106, China

(Received 21 July 2026; accepted 3 November 2026; published 16 November 2026)

We propose and numerically demonstrate a scheme for generating isolated attosecond soft x-ray pulses based on an enhanced self-amplified spontaneous emission configuration that employs a nondispersive inverse Cherenkov radiation dielectric laser accelerator (ICR-DLA) as the energy modulator. Unlike conventional modulators, whose dispersive resonance conditions distort few-cycle laser pulses, the ICR-DLA operates with a phase-matching condition strictly independent of the driving laser wavelength, thereby faithfully mapping the temporal waveform of the few-cycle pulse onto the longitudinal phase space of the electron beam. Start-to-end simulations show that a 2.5 GeV electron beam with a current of 3 kA and a normalized emittance of 0.43 mm · mrad, modulated by a 4 μm few-cycle laser pulse and subsequently compressed, generates a localized density profile comprising a few discrete microbunches. The dominant central spike attains a peak current of 12.1 kA and a duration of 1.5 fs and drives a nearly isolated soft x-ray pulse with a peak power of 10 GW and an full width at half maximum duration of 530 as, while the adjacent satellite pulses are suppressed to below 2 GW. By overcoming the fundamental bandwidth limitations of traditional modulators, this ICR-DLA-driven scheme provides a compact path toward next-generation attosecond x-ray free-electron lasers.

DOI: 10.1103/ptbx-fxbq

I. INTRODUCTION

The fundamental timescale of electronic processes—such as charge migration, electron correlation, and photoionization—lies in the attosecond regime [1,2]. Resolving these ultrafast dynamics in real time typically requires an isolated attosecond pulse to serve as a stroboscopic probe. Moreover, extending such probe pulses into the soft x-ray spectral region is highly desirable [3]. Soft x-rays uniquely cover the core-level absorption edges of many essential elements, providing simultaneous elemental and chemical-state specificity for probing complex molecular and solid-state systems [4]. Although tabletop high-harmonic generation (HHG) pioneered attosecond science and successfully delivered the first isolated attosecond pulses [5], its conversion efficiency decreases rapidly with increasing photon energy. Consequently, HHG-driven soft x-ray sources are generally restricted to the picojoule level. This severe photon flux deficit inherently limits the signal-to-noise ratio in time-resolved spectroscopy and essentially precludes single-shot investigations of irreversible processes or dilute samples [6,7]. To achieve high-fidelity attosecond transient absorption spectroscopy and single-shot precision, there is a pressing demand to develop advanced schemes capable of generating high-intensity, isolated attosecond soft x-ray pulses.

To bridge this intensity gap, x-ray free-electron lasers (XFELs) have emerged as the premier platform. By leveraging exponential gain mechanisms, state-of-the-art facilities such as the linac coherent light source (LCLS) and SwissFEL routinely deliver x-ray pulses with tens of gigawatts of peak power [8], outperforming tabletop HHG sources by several orders of magnitude. However, standard XFELs operate in the self-amplified spontaneous emission (SASE) regime, which fundamentally restricts the minimum achievable pulse duration. In the soft x-ray band,

[*]Contact author: zhangliwen@nuaa.edu.cn
[†]Contact author: liuwhao@nuaa.edu.cn

Published by the American Physical Society under the terms of the Creative Commons Attribution 4.0 International license. Further distribution of this work must maintain attribution to the author(s) and the published article's title, journal citation, and DOI.

the slippage between the radiation field and the electrons over a single gain length generally exceeds 1 fs [9], inherently constraining conventional SASE pulses to the femtosecond domain.

To break this femtosecond barrier, Zholents proposed the ESASE scheme [10]. This approach isolates an attosecond pulse through a precise sequence of longitudinal phase-space manipulations. First, a few-cycle external laser interacts with a relativistic electron beam inside a magnetic wiggler, inducing a resonant energy modulation. A downstream magnetic chicane then converts this energy chirp into a sharp density modulation, compressing a fraction of the electrons into a single, attosecond-scale current spike. Upon entering the main undulator, this ultrahigh current spike preferentially triggers exponential FEL amplification. Because it reaches saturation well before the uncompressed background beam, it selectively drives emission of an isolated attosecond x-ray pulse—a concept that has been successfully demonstrated at LCLS [11].

Despite the success of the conventional ESASE scheme, its reliance on a macroscopic magnetic modulator (wiggler) imposes inherent constraints on both the device footprint (typically several meters in length) and the required laser peak power (typically on the order of 10 GW) [12]. Recently, laser-driven dielectric microstructures have emerged as an alternative for advanced particle-beam manipulation, offering significant advantages in terms of compactness and energy efficiency [13,14]. The inverse Smith–Purcell dielectric laser accelerator (ISP-DLA) exploits femtosecond laser pulses to excite near-field evanescent waves that sustain longitudinal electric field strengths on the order of GV/m within micron-scale channels [15,16]. Over millimeter-scale interaction lengths, these intense fields are sufficient to induce energy modulations of several MeV in relativistic electron beams. Owing to this highly localized and enhanced field distribution, the dielectric microstructure approach requires roughly a factor of 10 less driving laser power than conventional magnetic wigglers [14].

However, when driven by the few-cycle laser pulses required for isolated attosecond pulse generation, both conventional magnetic wigglers and ISP-DLAs face a critical physical limitation: their resonance conditions are inherently dispersive [17,18]—i.e., the resonance condition depends on the laser wavelength, so different frequency components of the few-cycle pulse propagate at different phase velocities, which prevents the short temporal structure of the pulse from being fully transferred to the electron beam. To circumvent this, these modulators are forced into unfavorable trade-offs—such as drastically reducing the number of wiggler periods [19] or enlarging the ISP-DLA channel width [20]—to artificially broaden their acceptance bandwidth.

To overcome this fundamental dispersive bottleneck, we propose a novel energy modulation scheme based on the inverse Cherenkov radiation dielectric laser accelerator (ICR-DLA) [21–24]. The ICR-DLA not only inherits the millimeter-scale compactness and low driving-power requirements of the ISP-DLA but also possesses the key advantage of a nondispersive physical mechanism: the phase-matching condition is strictly independent of the driving laser wavelength [23]. Owing to this intrinsic nondispersive nature, the ICR-DLA can readily accommodate few-cycle laser pulses without sacrificing interaction length or near-field strength. By faithfully preserving the temporal envelope of the driving laser and imprinting a pristine, ultrashort energy modulation onto the relativistic electron beam, the ICR-DLA serves as an efficient and ideal modulator for the ESASE scheme, offering a robust path toward the generation of isolated attosecond soft x-ray pulses.

II. PROPOSED SCHEME

As illustrated in Fig. 1, the overall system layout comprises the upstream injector (omitted in the schematic), a matching section for the ICR-DLA, the ICR-DLA energy modulator, a magnetic chicane, a matching section for the undulator lattice, and the main radiation undulator. The relativistic electron beam from the injector is first transported through the upstream matching section and focused into the micron-scale channel of the ICR-DLA to ensure lossless transmission. Inside the ICR-DLA,

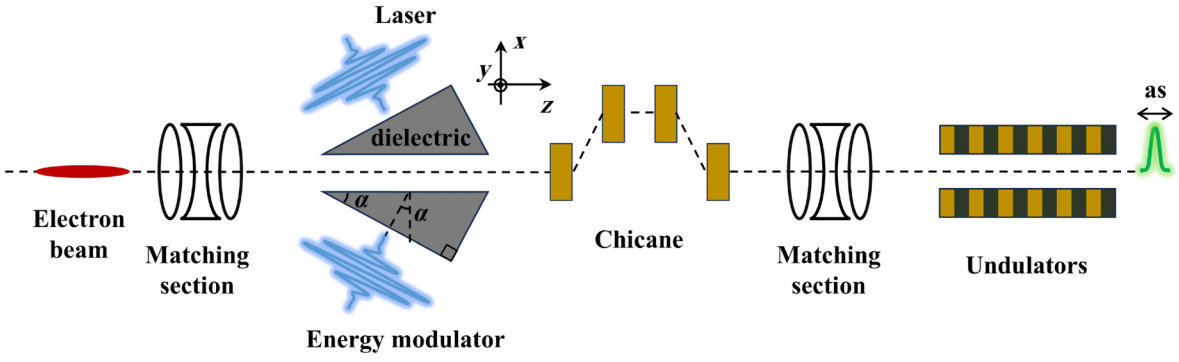


FIG. 1. Schematic layout of the proposed enhanced self-amplified spontaneous emission (ESASE) beamline.

which consists of opposing dielectric prisms, externally injected few-cycle driving lasers illuminate the structure to excite an optical near-field mode [21]. The phase-matching condition governing this interaction is given by:

$$\sin\alpha = \frac{1}{n\beta}, \tag{1}$$

where the synchronism condition depends exclusively on the laser incident angle α, the normalized electron velocity β, and the dielectric refractive index n, so that the resonance is inherently independent of the driving laser wavelength. The right-angle prism geometry is adopted primarily for practical optical alignment. As shown in Fig. 1, the driving laser enters the outer face of each prism at normal incidence, avoiding complex refraction at the first interface. Moreover, the portion of the laser pulse reflected from this normal-incidence face travels back along the incoming path, providing a direct experimental diagnostic to verify the correct incidence angle required by the synchronism condition in Eq. (1). By selecting Silicon (Si) as the dielectric material—which exhibits a nearly constant refractive index and a negligible extinction coefficient across the 1.8–7.0 μm spectral window (see Fig. 2). The wavelength-independent refractive index ensures that the phase-matching condition in Eq. (1) is strictly independent of the laser wavelength, and the negligible extinction coefficient means that the laser pulse propagates through the dielectric with negligible absorption loss.

Thus, the ICR-DLA acts as an ideal nondispersive modulator, faithfully imprinting the temporal waveform of the few-cycle laser onto the electron beam's longitudinal phase space. A downstream magnetic chicane then converts this energy modulation into a sharp density modulation. Because the imprinted modulation spans only a few optical cycles, this process generates a localized density profile consisting of a limited number of discrete microbunches, whose exact number and peak currents are strictly dictated by the laser's temporal field profile. Finally, the electron beam, now featuring a highly localized microbunch structure, passes through the downstream matching section to match its transverse Twiss parameters to the FODO lattice of the main undulator, where, via the ESASE mechanism, the radiation driven by the dominant current spike reaches saturation significantly earlier, thereby generating a nearly isolated attosecond soft x-ray pulse.

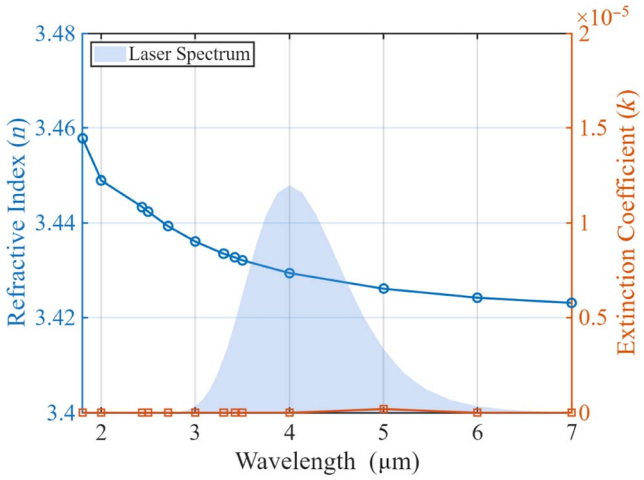


FIG. 2. Complex refractive index of Si [25] and the spectral profile of the driving laser (shaded area).

III. SIMULATIONS AND RESULTS

To provide a clear overview of the proposed setup, the key parameters of the driving laser, the ICR-DLA structure, the electron beam, the magnetic chicane, and the undulators are summarized in Table I. Based on these configurations, numerical simulations are carried out in the following sections.

TABLE I. Simulation parameters.

Parameter	Symbol	Value
Laser pulses		
Central wavelength	λ	4 μm
Peak amplitude	E_0	1.4 GV/m
Pulse duration	τ	20 fs
Carrier-envelope phase (CEP)	φ	90°
Incident angle	α	16.95°
ICR-DLA structure		
Dielectric material		Si
Channel width in x	g	4 μm
Channel width in y	w	200 μm
Structure length	L	2 mm
Electron beam		
Beam energy	E_k	2.5 GeV
Initial peak current	I_0	3 kA
Bunch length	Δt_0	100 fs
Rms relative energy spread	σ_δ	1×10^{-4}
Normalized emittance[a]	ε_n	0.43 mm · mrad
Chicane		
Longitudinal dispersion	R_{56}	1.3 mm
Dipole length	L_m	0.3 m
Drift length between first and second dipole	L_d	2 m
Bending angle	θ	0.985°
Undulators and FODO lattice		
Undulator period	λ_u	3 cm
Undulator parameter	K	1.09
Undulator module length	L_{mod}	3 m
Undulator module spacing	L_{drift}	0.5 m
Quadrupole strength	k_q	$\pm 2\,\mathrm{m}^{-2}$
Quadrupole length	ℓ_q	0.1 m

[a]Assumed to be the same in both transverse planes.

A. Electromagnetic field simulation in the ICR-DLA

To thoroughly evaluate the proposed scheme, we first perform electromagnetic simulations of the ICR-DLA structure. The simulations are conducted using a commercial electromagnetic code based on the finite-difference time-domain (FDTD) algorithm [26]. The incident few-cycle driving laser pulse is defined by the temporal profile:

$$E = E_0 \exp\left(-2\ln 2\frac{t^2}{\tau^2}\right)\cos(\omega t + \varphi), \tag{2}$$

where E is the total electric field of the incident laser pulse, $E_0 = 1$ is the normalized peak amplitude, $\tau = 20$ fs is the full width at half maximum (FWHM) duration, and the central wavelength is set to $\lambda = 4$ μm. The spectrum of this pulse lies well within the 1.8–7.0 μm window, as shown in Fig. 2, where silicon exhibits nearly constant n and negligible k. Crucially, the CEP is locked at $\varphi = 90°$. This CEP setting ensures that the zero-crossing of the electric field coincides precisely with the carrier-envelope peak of the laser pulse, which maximizes the longitudinal field gradient and thus the resulting energy modulation amplitude imparted to the electron beam. As discussed previously, Si is selected as the prism material. The channel width (vacuum gap in the x direction) is set to 4 μm. To fulfill the synchronism condition in Eq. (1) for relativistic electrons ($\beta \approx 1$), the laser incident angle is configured at $\alpha = 16.95°$.

Figure 3 shows the simulated longitudinal electric field $E_z(t)$ recorded at the center of the vacuum channel ($x = 0$) at three longitudinal positions ($z = 50$, 100, and 150 μm). Close examination of the temporal waveforms reveals that the excited near-field mode perfectly inherits the ultrashort envelope of the driving laser and remains well preserved along the channel with no noticeable dispersive broadening or distortion. The time delay of the near-field signal between adjacent observation points (spaced by $\Delta z = 50$ μm) is exactly $\Delta t = \Delta z/c$, where c is the speed of light in vacuum. This demonstrates that all frequency components of the broadband few-cycle pulse propagate with a phase velocity identically equal to c along the channel, confirming the nondispersive nature of the ICR-DLA.

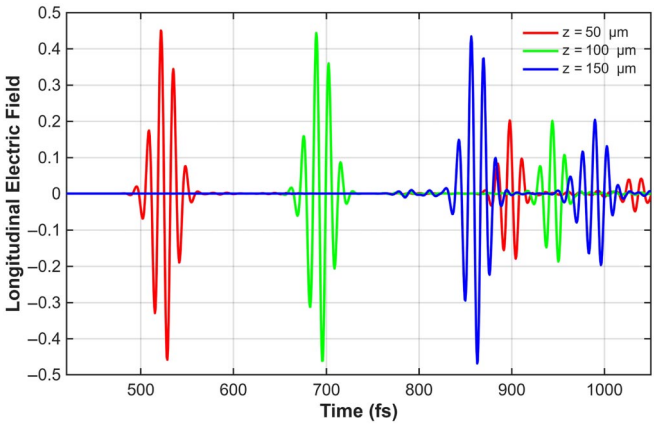


FIG. 3. E_z as a function of time at the center of the ICR-DLA channel ($x = 0$), recorded at three longitudinal positions: $z = 50$ μm (red), 100 μm (green), and 150 μm (blue).

Additionally, a trailing, smaller-amplitude field signal is observed in Fig. 3. This secondary pulse originates from the optical reflection at the prism interfaces. Analysis of its propagation delay yields an equivalent phase velocity of approximately $3.63c$. Because this phase velocity is significantly mismatched with the velocity of the relativistic electrons, the net energy modulation induced by this reflected field averages to zero over the interaction length, rendering its effect negligible. Finally, the FDTD simulation indicates that the peak amplitude of the effective longitudinal modulation field is approximately 0.45 E_0. These high-fidelity time-domain near-field data are then exported as electromagnetic field maps for the subsequent particle tracking.

B. Particle tracking simulation

To model the complete beam dynamics, we employ a combination of the general particle tracer (GPT) [27] and ELEGANT codes [28]. GPT is utilized to simulate the energy modulation within the ICR-DLA, as it supports the import of external spatiotemporal electromagnetic field maps. Specifically, a time series of the 3D field distribution on a spatial grid—i.e., $E(x, y, z, t), B(x, y, z, t)$—is dumped from the FDTD simulation and directly imported into GPT. No approximation or analytical reconstruction is employed; GPT tracks the particles by interpolating these fields both spatially and temporally from the imported data. This enables an accurate simulation of the interaction between the ultrashort laser pulse and the electron beam inside the ICR-DLA structure. In addition to the longitudinal energy modulation, this approach includes all transverse field components and thus accounts for any potential transverse focusing or defocusing effects. In practice, however, as derived in our previous work [21], the transverse electric and magnetic forces acting on the ultrarelativistic beam cancel each other out, resulting in no significant focusing or defocusing effects in the ICR-DLA. It should be noted that the structure-induced wakefields are not included in the GPT tracking. However, the 2D analysis in Appendix B shows that the longitudinal wakefield only causes a small, uniform energy loss that can be readily compensated, and the transverse wakefield is negligible. Thus, neglecting these wakefields is justified for the present study.

Subsequently, ELEGANT is employed to track the beam through the magnetic chicane, which is a well-established code widely used for beam transport through magnetic compressors and offers higher computational efficiency for large-scale tracking [28]. ELEGANT includes models

for both coherent synchrotron radiation (CSR) and longitudinal space charge (LSC), both of which were included in our simulations. While ELEGANT employs a 1D CSR model, it has been extensively benchmarked and accepted as reliable for predicting emittance degradation and longitudinal phase-space dynamics in such configurations [29,30].

The initial electron beam parameters at the entrance of the matching section are set to an energy of 2.5 GeV, an rms relative energy spread of 10^{-4}, a normalized emittance of 0.43 mm · mrad (taken as the same in both transverse planes as a simplifying assumption), and a peak current of 3 kA, which are adopted directly from the nominal operating parameters of the SwissFEL facility [31] and have been established as benchmarks in the recent attosecond FEL research [32]. The incident driving laser field amplitude is chosen as $E_0 = 1.4$ GV/m, a value carefully chosen to remain below the optical damage threshold of the Si prisms [33]. With a microchannel length of $L = 2$ mm and an effective longitudinal modulation field amplitude of $0.45E_0$ obtained from the FDTD simulations, the maximum energy modulation amplitude is estimated to be $\Delta E \approx e \cdot 0.45E_0 \cdot L = 1.26$ MeV. To prevent beam loss within the highly confined 4-μm-wide channel (defined as the x direction in our coordinates), stringent constraints are placed on the transverse emittance. The transverse acceptance of the ICR-DLA can be approximated as $A \approx g^2/L$ [34]. The condition for lossless transmission requires

$$\pi\epsilon_n/(\beta\gamma) < g^2/L, \tag{3}$$

where ϵ_n is the normalized transverse emittance, β is the normalized electron velocity, γ is the relativistic Lorentz factor, g is the channel width, and L is the channel length. Given these beam and channel parameters, Eq. (3) yields a maximum allowable normalized emittance of approximately 12.5 mm · mrad, well above the value of 0.43 mm · mrad used in our simulations.

The detailed beam optics design is provided in the Appendix. For the initial matching into the ICR-DLA, strong focusing quadrupoles are employed to produce a pronounced asymmetric waist. As illustrated in Fig. 4(a), the beam is focused at the channel center to reach rms sizes of $\sigma_x = 0.66$ μm and $\sigma_y = 29.64$ μm in the x and y planes, respectively. This sufficiently small rms size in the x direction guarantees that the beam envelope remains consistently smaller than the channel width over the entire 2 mm propagation length, as shown in Fig. 4(b). The ICR-DLA has a planar geometry: the channel is much narrower in the x direction than in the y direction, so the x direction is the critical constraint. As long as the beam is well confined in the x direction, lossless transmission is achieved. The electron beam size in the y direction can be significantly larger than that in the x direction. This substantially alleviates the impact of wakefield effects [35], which could otherwise induce beam instability or cause catastrophic damage to the dielectric material.

Following the ICR-DLA interaction, the simulated LPS of the electron beam is presented in Fig. 4(c). The LPS geometry closely mirrors the few-cycle temporal profile of the driving laser pulse. Furthermore, the maximum energy

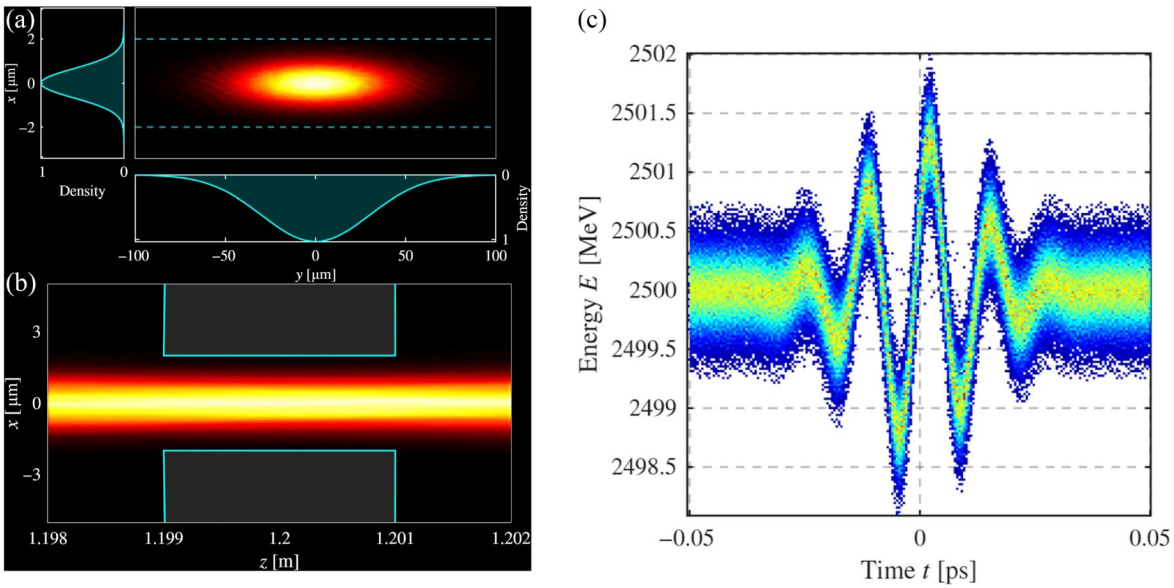


FIG. 4. Transverse profiles and LPS of the electron beam in the ICR-DLA. (a) Electron trajectories $x(z)$, with brightness indicating electron density and cyan lines denoting prism boundaries. (b) Transverse $x-y$ distribution at the channel center. Dashed lines represent the channel boundaries; left and bottom insets show 1D projected distributions along the x and y directions, respectively. (c) LPS distribution of the electron beam at the ICR-DLA exit.

modulation extracted from the particle tracking is approximately 1.23 MeV, aligning remarkably well with the estimate of 1.26 MeV. This further confirms the nondispersive nature of the ICR-DLA as an energy modulator.

The particle distribution exported from GPT is imported into ELEGANT to track the beam through the downstream magnetic chicane, converting the energy modulation into a density modulation. To obtain the shortest microbunch after the chicane, the longitudinal dispersion R_{56} must satisfy the optimal compression condition:

$$R_{56}k_L\frac{\Delta\gamma}{\gamma_0}=1, \tag{4}$$

where k_L is the wave number corresponding to the central laser wavelength, $\Delta\gamma$ is the energy modulation amplitude in units of the electron rest energy, and γ_0 is the average Lorentz factor of the beam. From the energy modulation amplitude obtained in the GPT simulation, the required R_{56} is calculated to be 1.3 mm. For a standard four-dipole chicane, R_{56} is given by [36]:

$$R_{56}=2\theta^2\left(L_d+\frac{2}{3}L_m\right), \tag{5}$$

where θ is the bending angle of the dipoles, L_d is the drift length between the first and second dipole, and L_m is the effective length of each dipole. With $L_m=0.3$ m and $L_d=2$ m, the required bending angle is calculated to be $\theta=0.985°$.

Figure 5 shows the beam properties at the exit of the chicane. To isolate collective effects, we first consider an ideal scenario with CSR and LSC turned off, as shown in Figs. 5(a)–5(c). The LPS in Fig. 5(a) clearly shows that the central electrons, having experienced the maximum energy modulation, are fully compressed into an upright rectangular distribution. By contrast, the adjacent regions with weaker modulation remain undercompressed. This optimal localized compression generates an intense microbunch at the bunch center, with a peak current of 13.6 kA and a duration of 1.4 fs. However, the compression process itself—through the conservation of longitudinal phase-space area—maps the energy chirp into an increased slice energy spread. As a result, the relative slice energy spread of the microbunch reaches approximately 3.5×10^{-4}, while the slice emittance remains largely unaffected.

When collective effects (including both CSR and LSC) are enabled, as depicted in Figs. 5(d)–5(f), the LPS reveals noticeable electron energy loss, particularly in the region

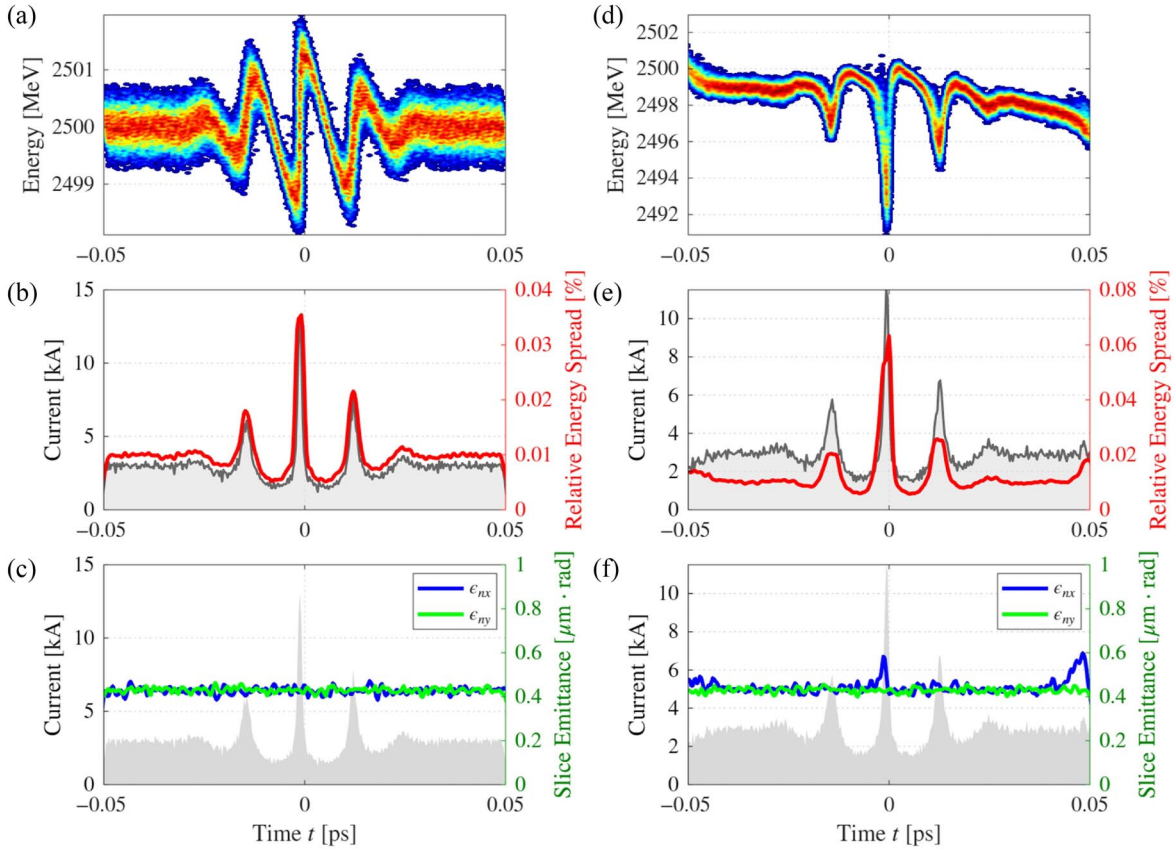


FIG. 5. ELEGANT simulation results of the electron beam at the chicane exit. (a)–(c) Ideal case with collective effects turned off: (a) LPS, (b) current profile and slice energy spread, and (c) slice emittance. (d)–(f) Realistic case with collective effects turned on: (d) LPS, (e) current profile and slice energy spread, and (f) slice emittance.

where the current is highest. This collective-effect-induced degradation slightly broadens the microbunch duration to 1.5 fs and reduces the peak current to 12.1 kA. Furthermore, the localized slice energy spread and the normalized slice emittance at the current peak increase to 6×10^{-4} and 0.53 mm · mrad, respectively. By contrast, the normalized slice emittance of the two adjacent satellite spikes exhibits no noticeable degradation, remaining close to the initial value of 0.43 mm · mrad. To confirm that the degraded beam still supports high-gain FEL amplification, we evaluate the FEL Pierce parameter ρ [17]. Assuming an rms transverse beam size of 30 μm, an undulator parameter of $K = 1.09$, and an undulator period of $\lambda_u = 3$ cm, the Pierce parameter is $\rho \approx 2.1 \times 10^{-3}$. This confirms that the final slice energy spread (6×10^{-4}), although elevated by the energy modulation and CSR effect, remains well below ρ. Thus, the microbunch fully satisfies the energy spread requirement for high-gain FEL amplification.

C. FEL simulation

The FEL simulation is performed using the time-dependent 3D code Genesis [37], taking the particle distribution exported from ELEGANT as the input. The undulator has a period of 3 cm and an undulator parameter of $K = 1.09$. According to the FEL resonance relation, the corresponding radiation wavelength is approximately 1 nm, falling within the soft x-ray regime. The undulator line consists of 3-m-long modules separated by 0.5-m drift sections that accommodate the quadrupoles to form a FODO lattice. The quadrupoles have an effective length of $l_q = 0.1$ m and a geometric strength of $k_q = \pm 2$ m^{-2}, giving a focal length of $f = 1/(|k_q| l_q) = 5$ m. With a FODO half-period of $L_{\mathrm{lat}} = 3.5$ m, the average beta function is $\hat{\beta} = L_{\mathrm{lat}}\kappa^2/\sqrt{\kappa^2 - 1} = 10.68$ m, where $\kappa = 2f/L_{\mathrm{lat}}$. The corresponding average transverse rms beam size is $\sigma_b = \sqrt{\hat{\beta}\varepsilon} \approx 30$ μm.

Since the peak current of the microbunch exceeds 10 kA, the LSC effect may not be negligible. We calculate the LSC wakefield based on the impedance model [38]:

$$Z_{\mathrm{lsc}}(k) = \frac{iZ_0}{\pi k r_b^2}\left[1 - \frac{kr_b}{\gamma} K_1\left(\frac{kr_b}{\gamma}\right)\right], \tag{6}$$

where Z_0 is the impedance of free space, $r_b \approx 2\sigma_b$ is the beam radius, k is the wave number, and K_1 is the modified Bessel function of the second kind of order 1. The LSC wakefield is obtained by the inverse Fourier transform of the product of $Z_{\mathrm{lsc}}(k)$ and the Fourier-transformed current profile $\lambda(k)$. Figure 6 illustrates the calculated LSC wakefield. The wakefield is strongly localized, reaching a peak amplitude of approximately 0.2 MV/m around the dominant microbunch with the highest peak current. This wakefield induces an additional energy chirp across the current spike, which detunes the beam from the FEL resonance condition and thereby degrades the radiation performance. In the unmodulated regions, the wakefield is negligible. The transverse space-charge effect, which mainly influences the transverse emittance, is not included in our simulations. This is consistent with previous ESASE studies [39], where transverse space-charge effects are shown to be negligible for similar beam parameters, and the longitudinal space-charge effect is treated as the dominant collective effect. Therefore, the LSC effect is incorporated into the Genesis simulations by importing the calculated wakefield distribution.

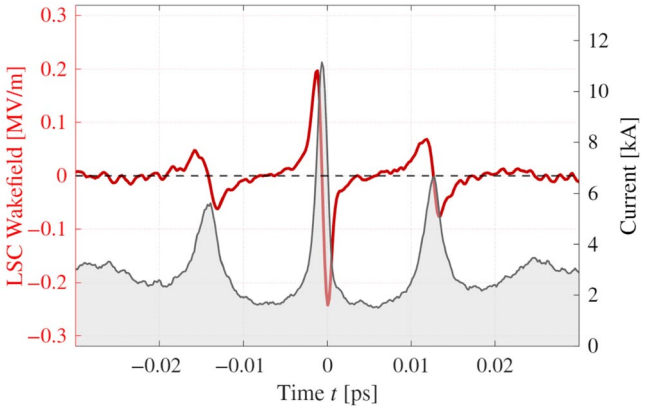


FIG. 6. The calculated LSC wakefield and the corresponding beam current profile.

The longitudinal current profile exhibits three microbunches resulting from the localized density modulation. The corresponding radiation pulses, denoted as Peak 1, Peak 2, and Peak 3, are individually tracked. Figure 7(a) shows the evolution of the peak radiation power along the undulator for these three microbunches. According to 1D FEL theory, the gain length scales inversely with the cube root of the local peak current ($L_g \propto I^{-1/3}$). Consequently, the central microbunch (Peak 2), which carries the highest peak current, has the shortest gain length $L_g \approx 1.3$ m and reaches saturation first, at an undulator distance of $z = 24.9$ m. At this point, the radiation driven by the adjacent parasitic microbunches (Peak 1 and Peak 3) is still in the exponential growth regime. If the undulator is terminated at this position, the output radiation is dominated by Peak 2. Because the satellite pulses (Peak 1 and Peak 3) are far from saturation and their power levels remain much lower, this approach naturally yields a nearly isolated single-spike pulse.

Figure 7(b) shows the radiation power profile at the saturation point ($z = 24.9$ m). Three distinct radiation pulses are generated, corresponding to the three microbunches, and their power levels far exceed the background emission from the unmodulated beam. The characteristic FEL slippage effect is clearly visible as the radiation pulses are shifted forward in the longitudinal coordinate relative

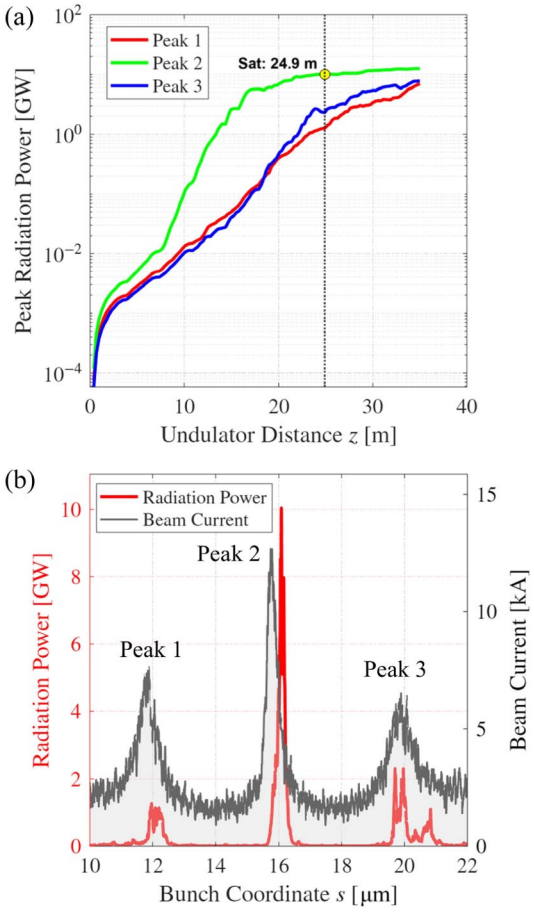


FIG. 7. (a) Peak radiation power versus undulator distance for the three microbunches. Peak 2 saturates first at $z = 24.9$ m. (b) Longitudinal profile of the radiation power and the electron beam current at $z = 24.9$ m.

to the current peaks. The primary pulse, driven by Peak 2, has a peak power of 10 GW and a FWHM duration of 530 as. In contrast, the satellite pulses (Peak 1 and Peak 3) are suppressed to below 2 GW, yielding a main-to-satellite peak-power contrast ratio of approximately 5. This good contrast demonstrates the feasibility of generating a nearly isolated attosecond soft x-ray pulse.

D. Comparison with wiggler-based modulators

To quantify the advantage of the proposed ICR-DLA modulator over conventional wiggler-based modulators, we fix the target energy modulation amplitude to that obtained in the ICR-DLA simulation, $\Delta E \approx 1.23$ MeV, and compare the driving laser power required to reach this same modulation in a conventional magnetic wiggler. The key figure of merit here is not only the required driving laser peak power but also the spectral acceptance bandwidth for a few-cycle driving pulse, since the latter determines whether the temporal waveform of the laser can be faithfully imprinted onto the electron beam. The underlying reason is the dispersive acceptance bandwidth of the wiggler. For a wiggler with N_w periods, the acceptance bandwidth scales approximately as $\Delta\omega/\omega \sim 1/N_w$. For the driving pulse used here, with central wavelength $\lambda = 4$ μm and FWHM duration $\tau = 20$ fs, the transform-limited relative bandwidth is $\Delta\omega/\omega \approx 30\%$. When interacting with such a broadband pulse, traditional wigglers face a physical bottleneck: attempting to lower the peak-power requirements by increasing the interaction length (adding more periods) inevitably shrinks the acceptance bandwidth, ultimately truncating the laser's spectrum and distorting the profile of the energy modulation imprinted on the electron beam.

To verify the above analysis, we compare the conventional wiggler modulator with the proposed ICR-DLA scheme by calculating the longitudinal phase-space modulation for three representative wiggler configurations. For all three cases, the wiggler period and wiggler parameter are fixed at $\lambda_w = 0.2$ m and $K = 43.74$, while the number of periods is chosen as $N_w = 1, 3$, and 5, corresponding to relative acceptance bandwidths of approximately 100%, 33%, and 20%, respectively. For each configuration, the driving field amplitude is rescaled so that the peak energy modulation matches the ICR-DLA value $\Delta E \approx 1.23$ MeV. The laser field is modeled as a Gaussian pulse including diffraction over long distances, with the radial dependence neglected because the laser waist is assumed to be large compared with the electron beam:

$$E_x(z,t) = \frac{E_0}{\sqrt{1+(z/z_R)^2}} \sin\left[\omega(z/c - t) + \psi\right] \times e^{-(z-ct)^2/(2c\sigma_t)^2}, \tag{7}$$

with $\psi = -\arctan(z/z_R) + \varphi$, where z_R is the Rayleigh length and σ_t is the rms duration. The energy modulation induced by this finite-duration laser pulse is expressed as [36]:

$$\Delta\gamma = \frac{2}{m_0 c^2}[JJ]\sqrt{A\alpha_f h\omega\xi} f(q,\nu,\tau_1,s)\cos(\omega s/c + \varphi), \tag{8}$$

with

$$[JJ] = J_0(\xi/2) - J_1(\xi/2), \tag{9}$$

$$f(q,\nu,\tau_1,s) = \sqrt{\frac{2q}{\sqrt{2\pi}\tau_1}} \int_{-1/2}^{1/2} \frac{\cos\left[2\pi\nu\hat{z} - \arctan(q\hat{z})\right]}{\sqrt{1+(q\hat{z})^2}} \times e^{-(\hat{z}/\tau_1 - s/c\sigma_t)^2/4} d\hat{z}, \tag{10}$$

$$\nu = \frac{2N_w(\gamma-\gamma_0)}{\gamma_0}, \quad q = \frac{N_w\lambda_w}{z_R}, \quad \tau_1 = \frac{c\sigma_t}{N_w\lambda}, \tag{11}$$

TABLE II. Parameters of the wiggler modulator.

Parameter	Symbol	Value
Electron beam energy	E_k	2.5 GeV
Target energy modulation	ΔE	1.23 MeV
Wiggler period	λ_w	0.2 m
Wiggler parameter	K	43.74
Number of wiggler periods	N_w	1, 3, 5
Laser central wavelength	λ	4 μm
Laser FWHM duration	τ	20 fs
Laser beam waist	w_0	1.5 mm
Peak amplitude	E_0	2.12, 0.98, 0.86 GV/m

where m_0 is the electron rest mass, $\xi = K^2/(2+K^2)$, $A = P\sqrt{2\pi}\sigma_t$ is the laser pulse energy, $P = \pi w_0^2 E_0^2/4Z_0$ is the peak laser power, w_0 is the laser waist, $\alpha_f = e^2/4\pi\varepsilon_0 hc$ is the fine structure constant, and h is Planck's constant.

To ensure that the laser field is approximately uniform across the electron beam trajectory, the laser beam waist w_0 must be significantly larger than the transverse range of the electrons. In the wiggler, the large parameter $K = 43.74$ induces a maximum transverse displacement of $x_{\max} = K\lambda_w/(2\pi\gamma) \approx 285$ μm. Considering the electron beam rms size of $\sigma_b \approx 30$ μm, the transverse boundary of the beam extends well beyond 300 μm from the axis. To maintain the laser field amplitude drop to within a few percent across this entire wiggling trajectory, the laser waist is set to $w_0 = 1.5$ mm. The parameters used are summarized in Table II.

Figure 8 shows the calculated LPS distributions and corresponding compressed current profiles for the three wiggler configurations. For the single-period wiggler ($N_w = 1$), the relative acceptance bandwidth of 100% far exceeds the 30% bandwidth of the driving laser. As shown in Fig. 8(a), the electron beam can thus accurately map the few-cycle temporal envelope of the driving laser. After chicane compression, this yields a sharp central current spike reaching 13.6 kA, accompanied by lower-amplitude satellite peaks with peak currents of approximately 7 kA [Fig. 8(d)]—a current profile comparable to that obtained with the proposed ICR-DLA scheme. However, this wiggler-based modulation requires a high driving laser power. To compensate for the short interaction length, a peak electric field as high as 2.12 GV/m is required. For a beam waist of 1.5 mm, this corresponds to a peak driving laser power exceeding 21 GW, which places stringent demands on the driving laser system, especially for high-repetition-rate operation.

Attempting to reduce this high power requirement by extending the interaction length reveals the inherent dispersive bottleneck of traditional wigglers. For $N_w = 3$, the required peak field decreases to 0.98 GV/m, corresponding to a peak power of approximately 4.5 GW, but the relative acceptance bandwidth narrows to 33%, comparable to the laser bandwidth. As shown in Fig. 8(b), the narrow bandpass filter effect begins to truncate the laser spectrum, visibly stretching the temporal envelope of the energy modulation. Consequently, the adjacent modulations are enhanced, degrading the compressed current

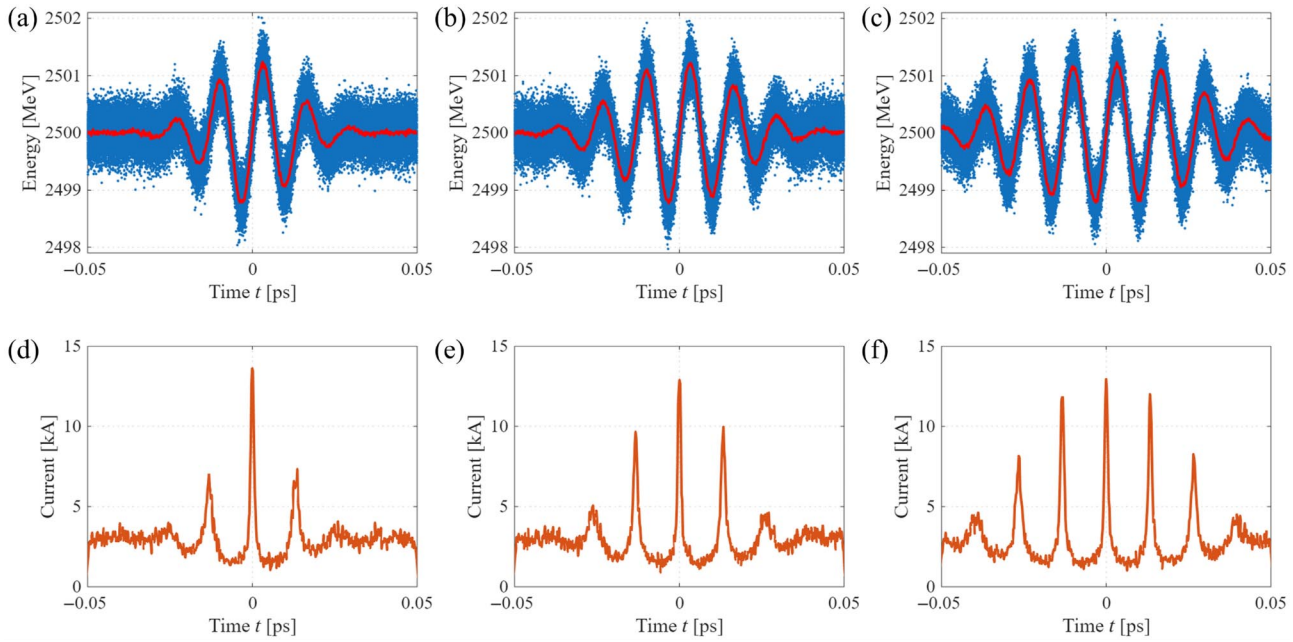


FIG. 8. LPS distributions (top row) and corresponding current profiles after chicane compression (bottom row) for an electron beam modulated in a conventional wiggler. The columns correspond to different numbers of wiggler periods: $N_w = 1$ (a),(d), $N_w = 3$ (b),(e), and $N_w = 5$ (c),(f). The red solid lines in panels (a)–(c) represent the slice-averaged energy.

profile: the satellite current peaks grow noticeably, reaching nearly 10 kA [Fig. 8(e)].

This dispersive distortion becomes catastrophic for the $N_w = 5$ configuration. Although the required peak field further decreases to 0.86 GV/m, corresponding to a peak power of approximately 3.5 GW, this reduction is marginal compared with the drop from 21 GW at $N_w = 1$ to 4.5 GW at $N_w = 3$. Meanwhile, the relative acceptance bandwidth narrows to 20%, smaller than the laser bandwidth. As a result, severe phase-matching breakdown occurs. The temporal envelope of the energy modulation is markedly smoothed and elongated, entirely losing its few-cycle characteristics [Fig. 8(c)]. After compression, the localized attosecond structure is destroyed and degenerates into a multicycle microbunch train, in which the parasitic satellite peaks reach nearly the same peak current as the central spike, about 12 kA [Fig. 8(f)]. Under these conditions, generating an isolated attosecond x-ray pulse becomes impossible, since the adjacent microbunches would inevitably drive competitive FEL emission.

In summary, the conventional wiggler modulator imposes a trade-off: one must either supply a high driving laser power (21 GW) or accept temporal distortions ($N_w \geq 3$) caused by bandwidth truncation. The proposed ICR-DLA circumvents both constraints. To maintain a uniform field along the 2 mm interaction length, the laser waist in the plane of incidence should be $w_{0,\parallel} \approx 2.95$ mm. In the vertical y direction, the laser only needs to cover the electron beam, whose rms size is $\sigma_y \approx 30$ μm, allowing the vertical waist to be tightly focused to $w_{0,y} \approx 277$ μm. At the required peak field amplitude of 1.4 GV/m, each driving laser requires a peak power of approximately 3.3 GW, for a total of about 6.6 GW. Thus, within a compact, millimeter-scale footprint, the ICR-DLA reduces the required peak laser power from 21 to 6.6 GW compared with the wiggler, while its inherently nondispersive phase-matching mechanism preserves the few-cycle temporal waveform.

IV. CONCLUSION

In summary, we have proposed and numerically demonstrated a novel scheme for generating isolated attosecond soft x-ray pulses, utilizing a compact ICR-DLA to overcome the dispersive bottlenecks of conventional energy modulators. Benefiting from strictly wavelength-independent phase-matching, the ICR-DLA precisely maps the few-cycle laser waveform onto the LPS of the electron beam. Subsequent magnetic compression converts this phase-space modulation into a highly localized current profile, featuring a dominant 1.5 fs, 12.1 kA microbunch. Driven by this ultrahigh local current, the FEL radiation reaches saturation significantly earlier, yielding a 10 GW, 530 as soft x-ray pulse at 1 nm. With adjacent satellite pulses inherently suppressed below 2 GW, the final output exhibits a good contrast, nearly isolated attosecond pulse. Operating within a millimeter-scale footprint, this nondispersive approach establishes a robust and viable technological route toward next-generation high-intensity attosecond light sources.

ACKNOWLEDGMENTS

This work was supported by the National Natural Science Foundation of China (Grants Nos. 12505163 and 12475153), the Key State Laboratory of Advanced Electromagnetic Technology (Grant No. AET 2025KF001), and the Key National Laboratory of Electromagnetic on Environment Effects of Science and Technology (Grant No. 6142205250201).

DATA AVAILABILITY

There are no publicly available research data or software supporting this manuscript. Requests for further information or data should be sent to the authors.

APPENDIX A: BEAM OPTICS DESIGN

This section details the complete beam optics design from the linear accelerator exit to the main undulator. The optics layout primarily involves two distinct matching sections: the focusing of the electron beam into the ICR-DLA structure and the subsequent matching into the undulator FODO lattice. The numerical optimization and particle tracking are performed using ELEGANT, with the overall evolution of the beta functions ($\hat{\beta}_{x,y}$) and dispersion (η_x) illustrated in Fig. 9.

To avoid beam loss, the beam inside the ICR-DLA channel must be well contained in both transverse directions. However, because the planar structure is much wider in the y direction, the x direction is the critical constraint. The maximum transverse beam size in the x direction must be strictly confined. The transmission condition dictates that the full beam width ($4\sigma_x$) must remain smaller than the

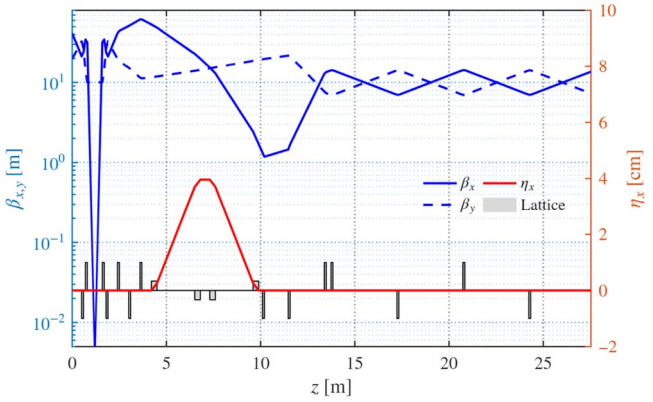


FIG. 9. Evolution of the beta functions ($\hat{\beta}_{x,y}$) and dispersion (η_x) along the complete beamline, optimized using ELEGANT.

channel gap g, yielding $2\sigma_{x,\max} < g/2$, where $\sigma_{x,\max}$ is the maximum rms beam size within the channel. Assuming the beam is focused to a waist exactly at the center of the structure, the Twiss parameter $\hat{\alpha}_0 = 0$. The longitudinal evolution of the beta function within the drift space of the channel is given by:

$$\hat{\beta}_x(z) = \hat{\beta}_0 + \frac{z^2}{\hat{\beta}_0}. \tag{A1}$$

Consequently, the maximum beta function occurs at the entrance and exit apertures of the structure. Substituting the relation $\sigma_x = \sqrt{\hat{\beta}_x \varepsilon_n/\gamma}$, the lossless transmission condition can be analytically expressed as:

$$\left(\hat{\beta}_0 + \frac{L^2}{4\hat{\beta}_0}\right)\frac{\varepsilon_n}{\gamma} < \frac{g^2}{16}. \tag{A2}$$

By substituting the beam parameters defined in the main text, the analytical upper limit for the waist beta function is determined to be $\hat{\beta}_0 < 11.3$ mm.

To realize this focal requirement, a defocusing-focusing-focusing-defocusing quadrupole configuration is employed. As depicted in the layout in Fig. 9, the ICR-DLA is positioned at the center between the two focusing quadrupoles. This configuration is mirror-symmetric: the upstream quadrupole pair focuses the electron beam into the ICR-DLA, while the downstream pair suppresses the severe beam divergence upon exiting the microchannel. The optimized geometric strengths of these quadrupoles are -28.8 and $40.0\ \mathrm{m}^{-2}$, respectively. Achieving such high field gradients necessitates the implementation of in-vacuum permanent magnet quadrupoles [40].

At the ICR-DLA center ($z = 1.2$ m), the optimized beta functions are $\hat{\beta}_x = 5$ mm and $\hat{\beta}_y = 10$ m. The horizontal beta function rigorously satisfies the theoretical requirement of $\hat{\beta}_0 < 11.3$ mm. Because the planar ICR-DLA structure has a significantly larger dimension in the y direction, $\hat{\beta}_y$ is permitted to be substantially larger. This design focuses the electron beam into a highly asymmetric waist, which perfectly accommodates the flat geometry of the microstructure.

Following the magnetic chicane, to achieve matching with the FODO lattice of the main undulator, it is necessary to first obtain the periodic Twiss solutions of the lattice. Considering the vertical focusing effect of the planar undulator, its equivalent geometric strength is defined as $k_y = 1/(2\rho^2)$, where $\rho = \gamma\lambda_u/(2\pi K)$ represents the bending radius of the electron trajectory in the undulator field. ELEGANT was utilized to optimize the geometric strengths of the lattice quadrupoles to equalize the phase advances in both transverse planes. The optimized quadrupole strengths are 2 and $-1.97\ \mathrm{m}^{-2}$. Under these lattice parameters, the periodic Twiss solutions at the entrance are evaluated as $\hat{\beta}_x = 14.17$ m, $\hat{\alpha}_x = -1.42$, $\hat{\beta}_y = 6.97$ m, and $\hat{\alpha}_y = 0.70$. With these target parameters established, standard electromagnetic quadrupoles are sufficient for the downstream matching section. As illustrated in Fig. 9, the segment from $z = 17.2$ m to $z = 24.2$ m corresponds to exactly one full FODO lattice period. The periodic oscillation of $\hat{\beta}_x$ and $\hat{\beta}_y$ in this region confirms that the precise matching into the undulator lattice has been successfully achieved.

APPENDIX B: WAKEFIELD ANALYSIS IN THE ICR-DLA

As described in the main text, the particle tracking within the ICR-DLA using the GPT code does not include structure-induced wakefields. To justify this treatment, we develop a 2D analytical model to evaluate the wakefields. The ICR-DLA has a planar geometry, and the focused electron beam is highly asymmetric and flat ($\sigma_y \gg \sigma_x$). Therefore, the 2D approximation (assuming infinite extent in the y direction) is physically reasonable. Figure 10 shows a schematic of the 2D model. The vacuum channel (region I) is bounded by two semi-infinite dielectric slabs (regions II and III). The electron beam is modeled as a line charge of density q moving along the $+z$ direction at a transverse offset x_0. Starting from Maxwell's equations in the frequency domain, the electric field E_z in the vacuum channel satisfies the inhomogeneous Helmholtz equation:

$$\nabla^2 E_z + k^2 E_z = j\omega\mu_0 J_z + \frac{1}{\epsilon_0}\frac{\partial \rho_e}{\partial z}, \tag{B1}$$

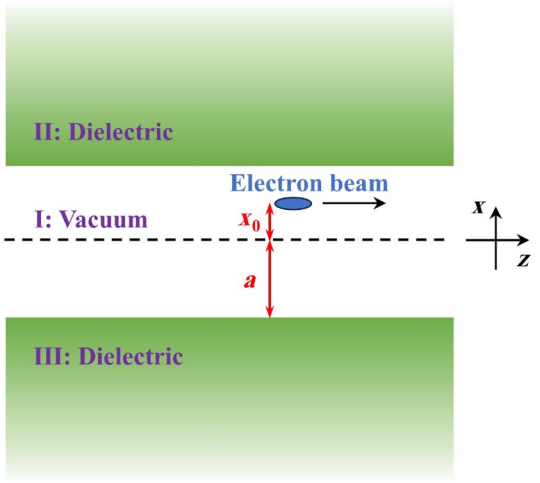


FIG. 10. Schematic of the 2D ICR-DLA model used for wakefield calculation.

where $k = \omega/c$ is the wave number in vacuum. The charge density ρ_e and longitudinal current density J_z are given by:

$$\begin{aligned}\rho_e &= q\delta(x-x_0)\frac{1}{v}e^{-j\omega z/v}\\ J_z &= q\delta(x-x_0)e^{-j\omega z/v}.\end{aligned} \tag{B2}$$

The solution for the fields in the vacuum channel is the superposition of the particular solution, representing the space-charge self-field of the source, and the homogeneous solution, representing the structure-induced wakefield. These are given by:

$$\begin{aligned}E_z^I &= j\frac{q\omega\mu_0}{2k_c\beta^2\gamma^2}e^{-k_c|x-x_0|-jk_z z}\\ &\quad+[B_1\cosh(k_c x)+B_2\sinh(k_c x)]e^{-jk_z z}\\ H_y^I &= \frac{q}{2}\frac{x-x_0}{|x-x_0|}e^{-k_c|x-x_0|-jk_z z}\\ &\quad+j\frac{\omega\epsilon_0}{k_c}[B_1\sinh(k_c x)+B_2\cosh(k_c x)]e^{-jk_z z},\end{aligned} \tag{B3}$$

where $k_c = \sqrt{k_z^2 - k^2}$ is the transverse decay constant, $k_z = \omega/v$ is the longitudinal wave number, and B_1 and B_2 are undetermined coefficients. In the semi-infinite dielectric regions, where no incoming waves exist, the fields propagate outward and are given by:

$$\begin{aligned}E_z^{(\mathrm{II})} &= C_1 e^{-j(k_x x+k_z z)}\\ H_y^{(\mathrm{II})} &= -\frac{\omega\epsilon_r\epsilon_0}{k_x}C_1 e^{-j(k_x x+k_z z)},\end{aligned} \tag{B4}$$

$$\begin{aligned}E_z^{(\mathrm{III})} &= D_1 e^{j(k_x x-k_z z)}\\ H_y^{(\mathrm{III})} &= \frac{\omega\epsilon_r\epsilon_0}{k_x}D_1 e^{j(k_x x-k_z z)},\end{aligned} \tag{B5}$$

where $k_x = \sqrt{\epsilon_r k^2 - k_z^2}$ is the transverse wave number in the dielectric, ϵ_r is the relative permittivity of the dielectric, and C_1 and D_1 are undetermined coefficients. At the vacuum-dielectric interfaces $x = \pm a$, the tangential components E_z and H_y are continuous. Applying these boundary conditions yields the undetermined coefficients:

$$\begin{aligned}B_1 &= -\frac{q\cosh(k_c x_0)e^{-k_c a}(j\epsilon_r k_c/k_x+1)}{2\omega\epsilon_0[\epsilon_r\cosh(k_c a)/k_x + j\sinh(k_c a)/k_c]}\\ B_2 &= -\frac{q\sinh(k_c x_0)e^{-k_c a}(j\epsilon_r k_c/k_x+1)}{2\omega\epsilon_0[\epsilon_r\sinh(k_c a)/k_x + j\cosh(k_c a)/k_c]}.\end{aligned} \tag{B6}$$

For a test particle trailing the driving charge at a distance s, the longitudinal wakefield can be obtained via the inverse Fourier transform of the structure-induced part of the E_z^I field:

$$w_\parallel = \frac{1}{2\pi}\int_{-\infty}^{+\infty}[B_1\cosh(k_c x)+B_2\sinh(k_c x)]e^{jk_z s}d\omega. \tag{B7}$$

Using the Panofsky–Wenzel theorem [41], the transverse wakefield is derived from the longitudinal wakefield:

$$w_\perp = \frac{1}{2\pi}\int_{-\infty}^{+\infty}\frac{v}{j\omega}k_c[B_1\sinh(k_c x)+B_2\cosh(k_c x)]e^{jk_z s}d\omega. \tag{B8}$$

For an electron beam with a normalized longitudinal distribution $\lambda(s)$, the wakefields are given by the convolution of the point-charge wakefields with the bunch distribution:

$$\begin{aligned}W_\parallel(s) &= \int_0^\infty w_\parallel(s')\lambda(s-s')ds'\\ W_\perp(s) &= \int_0^\infty w_\perp(s')\lambda(s-s')ds'.\end{aligned} \tag{B9}$$

Using the parameters listed in Table I, the longitudinal and transverse wakefields are calculated from Eqs. (B6)–(B9). The results are shown in Fig. 11. As shown in Fig. 11(a), the longitudinal wakefield $W_\parallel$ reaches a peak amplitude of approximately 2.1 GV/m within the bunch

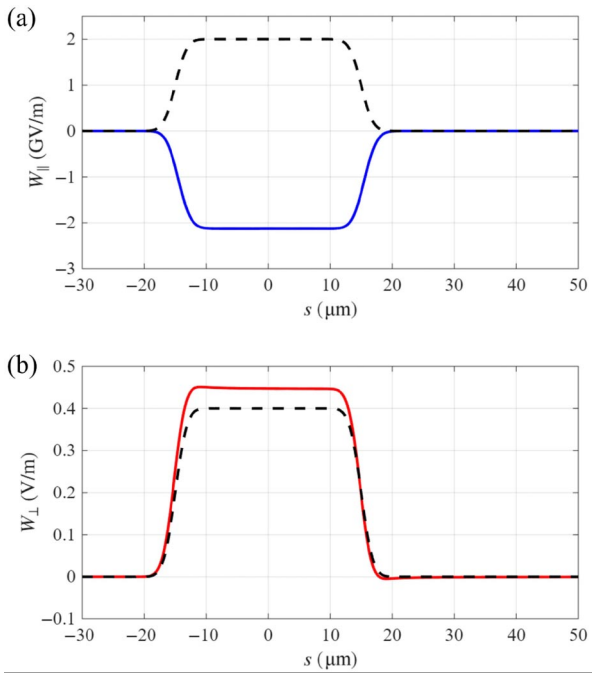


FIG. 11. Calculated (a) longitudinal and (b) transverse wakefields as functions of the distance s behind the driving charge for the ICR-DLA parameters listed in Table I. The black dashed lines represent the normalized electron beam distribution. The transverse wakefield in panel (b) is evaluated for a transverse beam offset $x_0 = 1$ μm.

core. Although this amplitude exceeds the laser-induced modulation field (0.63 GV/m), the wakefield is flat across the bunch and thus acts as a uniform deceleration. Consequently, it only reduces the overall beam energy without distorting the longitudinal phase space or affecting the energy modulation. Over the 2 mm interaction length, this corresponds to a global energy loss of about 4.2 MeV. Such a shift can be readily compensated by upstream linac tuning or a slight adjustment of the downstream undulator parameter K, ensuring that the FEL resonance condition is maintained.

Figure 11(b) shows the transverse wakefield $W_\perp$ for an electron beam with a transverse offset of $x_0 = 1$ μm. Its peak amplitude is only 0.45 V/m. The resulting transverse kick can be estimated as $\Delta x' \simeq eW_\perp L/E \approx 3.6 \times 10^{-13}$ rad, which is far smaller than the beam divergence (on the order of microradians). Thus, the transverse wakefield has a negligible influence on the beam dynamics. These results justify neglecting the wakefields in the present GPT tracking; a more rigorous 3D treatment will be considered in future work.

[1] P. B. Corkum and F. Krausz, Attosecond science, Nat. Phys. **3**, 381 (2007).

[2] F. Krausz and M. Ivanov, Attosecond physics, Rev. Mod. Phys. **81**, 163 (2009).

[3] S. R. Leone, C. W. McCurdy, J. Burgdörfer, L. S. Cederbaum, Z. Chang, N. Dudovich, J. Feist, C. H. Greene, M. Ivanov, R. Kienberger *et al.*, What will it take to observe processes in 'real time'?, Nat. Photonics **8**, 162 (2014).

[4] M. F. Ciappina, J. A. Pérez-Hernández, A. S. Landsman, W. A. Okell, S. Zherebtsov, B. Förg, J. Schötz, L. Seiffert, T. Fennel, T. Shaaran *et al.*, Attosecond physics at the nanoscale, Rep. Prog. Phys. **80**, 054401 (2017).

[5] M. Hentschel, R. Kienberger, C. Spielmann, G. A. Reider, N. Milosevic, T. Brabec, P. Corkum, U. Heinzmann, M. Drescher, and F. Krausz, Attosecond metrology, Nature (London) **414**, 509 (2001).

[6] E. J. Takahashi, P. Lan, O. D. Mücke, Y. Nabekawa, and K. Midorikawa, Attosecond nonlinear optics using gigawatt-scale isolated attosecond pulses, Nat. Commun. **4**, 2691 (2013).

[7] B. Bergues, D. Rivas, M. Weidman, A. Muschet, W. Helml, A. Guggenmos, V. Pervak, U. Kleineberg, G. Marcus, R. Kienberger *et al.*, Tabletop nonlinear optics in the 100-eV spectral region, Optica **5**, 237 (2018).

[8] N. Berrah, J. Cryan, R. Robles, T. Driver, A. Marinelli, and P. Bucksbaum, Attosecond X-ray sources, methods, and applications at present and future free-electron lasers: Tutorial, Adv. Opt. Photonics **17**, 623 (2025).

[9] N. Hartmann, G. Hartmann, R. Heider, M. Wagner, M. Ilchen, J. Buck, A. Lindahl, C. Benko, J. Grünert, J. Krzywinski *et al.*, Attosecond time–energy structure of X-ray free-electron laser pulses, Nat. Photonics **12**, 215 (2018).

[10] A. A. Zholents, Method of an enhanced self-amplified spontaneous emission for x-ray free electron lasers, Phys. Rev. ST Accel. Beams **8**, 040701 (2005).

[11] J. Duris, S. Li, T. Driver, E. G. Champenois, J. P. MacArthur, A. A. Lutman, Z. Zhang, P. Rosenberger, J. W. Aldrich, R. Coffee *et al.*, Tunable isolated attosecond X-ray pulses with gigawatt peak power from a free-electron laser, Nat. Photonics **14**, 30 (2020).

[12] A. A. Zholents, W. M. Fawley, P. Emma, Z. Huang, G. Stupakov, and S. Reiche, Current-enhanced SASE using an optical laser and its application to the LCLS, in *Proceedings of the 2004 FEL Conference* (JACoW Publishing, Geneva, Switzerland, 2004), p. 582, SLAC-PUB-10713.

[13] D. S. Black, U. Niedermayer, Y. Miao, Z. Zhao, O. Solgaard, R. L. Byer, and K. J. Leedle, Net acceleration and direct measurement of attosecond electron pulses in a silicon dielectric laser accelerator, Phys. Rev. Lett. **123**, 264802 (2019).

[14] B. Hermann, S. Bettoni, T. Egenolf, U. Niedermayer, E. Prat, and R. Ischebeck, Laser-driven modulation of electron beams in a dielectric micro-structure for x-ray free-electron lasers, Sci. Rep. **9**, 19773 (2019).

[15] E. Peralta, K. Soong, R. England, E. Colby, Z. Wu, B. Montazeri, C. McGuinness, J. McNeur, K. Leedle, D. Walz *et al.*, Demonstration of electron acceleration in a laser-driven dielectric microstructure, Nature (London) **503**, 91 (2013).

[16] J. Breuer and P. Hommelhoff, Laser-based acceleration of nonrelativistic electrons at a dielectric structure, Phys. Rev. Lett. **111**, 134803 (2013).

[17] E. L. Saldin, E. Schneidmiller, and M. V. Yurkov, *The Physics of Free Electron Lasers* (Springer Science & Business Media, Berlin, Heidelberg, 2013).

[18] R. J. England, R. J. Noble, K. Bane, D. H. Dowell, C.-K. Ng, J. E. Spencer, S. Tantawi, Z. Wu, R. L. Byer, E. Peralta *et al.*, Dielectric laser accelerators, Rev. Mod. Phys. **86**, 1337 (2014).

[19] A. A. Zholents and G. Penn, Obtaining attosecond x-ray pulses using a self-amplified spontaneous emission free electron laser, Phys. Rev. ST Accel. Beams **8**, 050704 (2005).

[20] T. Plettner, P. P. Lu, and R. L. Byer, Proposed few-optical cycle laser-driven particle accelerator structure, Phys. Rev. ST Accel. Beams **9**, 111301 (2006).

[21] L. Zhang, W. Liu, Y. Liu, Q. Jia, B. Sun, H. Xu, and S. Liu, Inverse Cherenkov dielectric laser accelerator for ultra-relativistic particles, J. Phys. D **56**, 045103 (2023).

[22] L. Zhang, H. Xu, and W. Liu, Inverse Cherenkov dielectric laser accelerator with alternating phase focusing for subrelativistic particles, Phys. Rev. Accel. Beams **27**, 110401 (2024).

[23] W. Liu, Z. Yu, L. Sun, Y. Liu, Q. Jia, H. Xu, and B. Sun, Microscale laser-driven particle accelerator using the inverse Cherenkov effect, Phys. Rev. Appl. **14**, 014018 (2020).

[24] L. Zhang, W. Liu, H. Xu, S. Liu, and Y. Lu, Synchronous acceleration of subrelativistic particles in an inverse-Cherenkov dielectric laser accelerator with tapered phase velocity, IEEE Trans. Plasma Sci. **51**, 3484 (2023).

[25] E. Shkondin, O. Takayama, M. E. A. Panah, P. Liu, P. V. Larsen, M. D. Mar, F. Jensen, and A. V. Lavrinenko,

Large-scale high aspect ratio Al-doped ZnO nanopillars arrays as anisotropic metamaterials, Opt. Mater. Express **7**, 1606 (2017).

[26] CST Corp., CST PS Tutorials, Dassault Systèmes, [Online; Accessed November 2026].

[27] Pulsar Physics, General particle tracer [Online] (2023), http://www.pulsar.nl/gpt.,

[28] M. Borland, Elegant: A flexible SDDS-compliant code for accelerator simulation, Tech. Rep. LS-287, Advanced Photon Source, Argonne National Laboratory, Argonne, IL, USA, 2000.

[29] M. Borland, Simple method for particle tracking with coherent synchrotron radiation, Phys. Rev. ST Accel. Beams **4**, 070701 (2001).

[30] K. Bane, F.-J. Decker, Y. Ding, D. Dowell, P. Emma, J. Frisch, Z. Huang, R. Iverson, C. Limborg-Deprey, H. Loos *et al.*, Measurements and modeling of coherent synchrotron radiation and its impact on the linac coherent light source electron beam, Phys. Rev. ST Accel. Beams **12**, 030704 (2009).

[31] C. J. Milne, T. Schietinger, M. Aiba, A. Alarcon, J. Alex, A. Anghel, V. Arsov, C. Beard, P. Beaud, S. Bettoni *et al.*, SwissFEL: The Swiss X-ray free electron laser, Appl. Sci. **7**, 720 (2017).

[32] Y. Xiao, T. Chen, B. Liu, Z. Huang, M. Pang, Y. Leng, and C. Feng, Isolated attosecond free-electron laser based on a subcycle driver from hollow capillary fibers, Ultrafast Sci. **5**, 0099 (2025).

[33] K. Werner, V. Gruzdev, N. Talisa, K. Kafka, D. Austin, C. M. Liebig, and E. Chowdhury, Single-shot multi-stage damage and ablation of silicon by femtosecond mid-infrared laser pulses, Sci. Rep. **9**, 19993 (2019).

[34] A. Ody, P. Musumeci, J. Maxson, D. Cesar, R. J. England, and K. P. Wootton, Flat electron beam sources for DLA accelerators, Nucl. Instrum. Methods Phys. Res., Sect. A **865**, 75 (2017).

[35] D. Mihalcea, P. Piot, and P. Stoltz, Three-dimensional analysis of wakefields generated by flat electron beams in planar dielectric-loaded structures, Phys. Rev. ST Accel. Beams **15**, 081304 (2012).

[36] E. Hemsing, G. Stupakov, D. Xiang, and A. Zholents, Beam by design: Laser manipulation of electrons in modern accelerators, Rev. Mod. Phys. **86**, 897 (2014).

[37] S. Reiche, GENESIS 1.3: A fully 3D time-dependent FEL simulation code, Nucl. Instrum. Methods Phys. Res., Sect. A **429**, 243 (1999).

[38] Z. Huang, M. Borland, P. Emma, J. Wu, C. Limborg, G. Stupakov, and J. Welch, Suppression of microbunching instability in the linac coherent light source, Phys. Rev. ST Accel. Beams **7**, 074401 (2004).

[39] Y. Ding, Z. Huang, D. Ratner, P. Bucksbaum, and H. Merdji, Generation of attosecond x-ray pulses with a multicycle two-color enhanced self-amplified spontaneous emission scheme, Phys. Rev. ST Accel. Beams **12**, 060703 (2009).

[40] E. Prat, S. Bettoni, M. Calvi, M. Dehler, F. Frei, P. Hommelhoff, M. Kozak, J. McNeur, C. O. Loch, S. Reiche *et al.*, Outline of a dielectric laser acceleration experiment at SwissFEL, Nucl. Instrum. Methods Phys. Res., Sect. A **865**, 87 (2017).

[41] W. K. H. Panofsky and W. A. Wenzel, Some considerations concerning the transverse deflection of charged particles in radio-frequency fields, Rev. Sci. Instrum. **27**, 967 (1956).